



Programming polymorphable yet stiff truss metamaterials in response to temperature

Ruizhe Ma, Lu Liu, Omar Wyman, Damiano Pasini*

Department of Mechanical Engineering, McGill University, Montreal, Quebec H3A 0C3, Canada

ARTICLE INFO

Article history:

Received 23 December 2021

Revised 11 February 2022

Accepted 22 February 2022

Keywords:

Shape morphable stiff metamaterials

Programmable multimaterial trusses

Polymorphing

Temperature stimulus

ABSTRACT

Shape morphing in response to an external stimulus can create geometric transformations from initially flat materials. Current strategies rely on thin layers made of soft materials that are inherently floppy to provide morphability, but cannot support their own weight and must forgo structural resistance, hence limiting their use as structural materials. Here, we demonstrate thermally actuated shape morphing of a three-dimensional framework that can evolve into complex, lightweight shapes that are both stiff and morphable, hence resolving the conflict between rigidity and morphability. Our building block is a truss unit cell that leverages the mismatched thermal expansions of its rigid constituents to generate programmable spatial deformation. By encoding specific geometric and multimaterial attributes into the truss system, we realize shape morphing on target and generate reversible structural transformations with complex curvature combinations. We also explore cooling and localized heating, unveiling temperature-dependent morphological evolutions and heat-source tracking. The morphable, yet stiff, truss metamaterial here introduced has potential applications in thermally responsive smart buildings, thermal management adaptive devices, deployable shelters in extreme environments, and mirror optical systems in space.

© 2022 Elsevier Ltd. All rights reserved.

1. Introduction

Shape morphing in response to external stimuli is extensively observed in both the natural and synthetic worlds. Pine cones, for instance, disperse seeds by opening scales in response to changes in humidity [1], while flytraps capture prey through traps triggered by mechanical actuation [2]. Learning from nature, synthetic materials endowed with a certain degree of shape morphing have been carefully designed to attain specific responses and functionalities upon activation, e.g. amplified actuation [3,4], self-deployment [5,6], self-folding [7,8], autonomous locomotion [9,10], time-dependent control [11,12], and logic operation [13,14], that are often dissimilar from and beyond those of natural and conventional materials. Combined with these characteristics, shape morphing materials hold promise in a wide range of applications, including drug delivery [15,16], biomedical devices [17], smart textiles [18], space exploration [19], and autonomous robots [20,21].

Among several shape morphing systems, those capable of transforming flat configurations into complex 3D geometries, where material and geometric attributes are encoded into initially flat constructs, can attain predefined 3D shapes upon activation. Pro-

gramming 3D transformations from flat materials has relied on soft materials shaped in thin geometries that are inherently floppy, and mainly use two underlying principles: (i) out-of-plane bending in multilayered architectures, and/or (ii) instability triggered in flat matter. The former is generated by stress gradients throughout the thickness of the material, whereas the latter arises from in-plane compressive stresses caused by in-plane dimensional changes, as further explained below.

Out-of-Plane Bending. To create stress gradient throughout the material thickness, dissimilar materials, each with its own distinct response to a given stimulus, are typically tessellated in thin layered structures. For example, a bilayered hydrogel with differential swelling ratios has been used for self-folding [22] in an aqueous environment, and a trilayer construct with one shrinking layer sandwiched between two outer layers has been shown capable of bending deformation under an increase in temperature [8,11]. In general, the bending curvature of bilayers is programmable through manipulation of their geometric attributes, such as the thickness ratio [23,24], as well as material properties, such as the swelling (or expansion) ratio [22,24] and stiffness ratio [23,25]. For trilayer structures, bending magnitude can be programmed by rationally employing hinge gaps [8] or bumpers [11]. The deformation mode can also be adjusted to achieve 3D shape morphing. For example, either single curvature or doubly curved shapes can

* Corresponding author.

E-mail address: damiano.pasini@mcgill.ca (D. Pasini).

be programmed in bilayers made of isotropic materials by tuning the aspect ratio [26–28], thickness ratio [29,30], and stiffness ratio [29,30]. Introducing inclusions, oriented at a desired angle with respect to the main axis of isotropic or anisotropic bilayers, is another approach to generate morphed shapes such as rolls and cylindrical or twisted helices [31,32]. While 3D shape morphing from flat materials via out-of-plane bending has been widely reported, all concepts require laminate architecture, i.e. thin layered system, either bilayer or trilayer. Furthermore, more complex geometries with nonzero Gaussian curvatures beyond rolls, cylindrical and twisted helices, are uncommon.

Out-of-Plane Buckling. The generation of in-plane compressive stresses, which leads to out-of-plane buckling, is another approach used to attain 3D shape morphing. Unlike the bending strategy, in-plane compressive stresses are typically induced by tessellating dissimilar materials in a single layer. The resulting deformation mode is governed by the tessellation pattern. For example, liquid crystals can be aligned azimuthally or radially in a circular polymer film to form a cone or saddle shape upon heating [33], whereas hydrogels with distinct swelling ratios are tessellated in parallel for the generation of a rolling bi-strip with a transition area [34], or alternatively aligned at an angle to the long axis of the sheet to create a range of shapes; these include cylindrical, twisted or conical helix, configurations determined by the interplay between the oblique angle and strip widths gradient upon immersion in an aqueous medium [35]. More complex shapes have been obtained by encoding into the flat geometry the prescribed metric tensor, which describes the distance between neighboring points. When the flat construct undergoes in-plane dimensional changes upon activation, a desired level of stress can be achieved, and then released during morphing to minimize the elastic energy [36–38]. This approach, however, poses challenges in controlling the out-of-plane direction of deformation due to the instability induced by morphing. In-plane compressive stresses can also be induced mechanically by locally attaching a thin top layer to a pre-strained substrate, resulting in out-of-plane buckling if the substrate is released. For example, complex 3D structures can be produced at small length scales when planar semiconductor nanoribbons are subjected to compressive forces owing to the release of the pre-stretched substrate [39,40]. However, methods for inducing out-of-plane buckling are still limited to thin layers typically made of very soft and flexible materials.

In addition to the two underlying physical principles mentioned above, origami and kirigami approaches have been documented for 3D shape transformation; by rationally designing the crease and cut patterns flat sheets can transform into complex spatial geometries. For example, Dudte et al. [41] use Miura-ori tessellations to generate curved surfaces, such as a logarithmic spiral and a hyperbolic paraboloid, while non-periodic cut patterns are introduced into flat sheets, which buckle into 3D shapes, such as a dome shape and a wrinkle pattern, when pulled at specific regions [42]. However, origami and kirigami techniques are restricted to thin sheets, and manual folding, as well as control over the folding direction and angle, becomes increasingly challenging at smaller or larger length scales.

Here, we demonstrate a reversible, thermally actuated 3D shape morphing from an initially flat truss architecture made of multiple stiff solids. We introduce a truss-like unit cell that differs from all the thin layered architectures and other concepts in the literature, resulting in a weight-efficient structure. When subjected to temperature changes, the 3D unit cell built of multimaterials with distinct CTE¹ displays programmable spatial deformation governed by the mutual interaction of its truss members. A variety of meta-

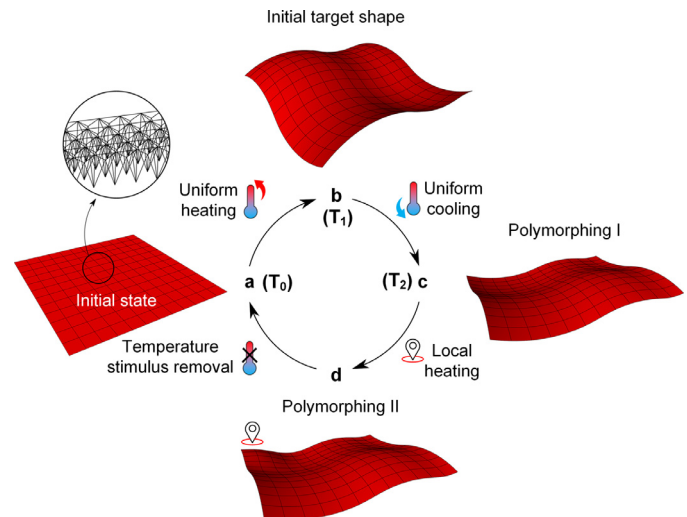


Fig. 1. Overview of temperature-induced 3D shape morphing of a truss system from an initially flat geometry. **a** Flat lattice assembled from encoded unit cells with programmed sequence and attributes of material and geometry. Inset shows the truss-like nature of the system. **b** Target shape attained by uniformly heating the flat lattice to a prescribed temperature T_1 ($T_1 > T_0$; initial temperature). **c** Inverted transformation of the target shape obtained by switching from uniform heating to cooling T_2 ($T_2 < T_0$), leading to a dissimilar configuration, namely Polymorphing I. **d** Localized deformation realized upon local application of stimulus, resulting in another shape modulation, namely Polymorphing II. Upon removal of all thermal stimuli, the morphed truss-like lattice returns to its initial geometry, thus exhibiting full morphing reversibility.

surfaces consisting of multiple unit cells, are created to match pre-defined shape targets, each attained via an encoded sequence of material and geometric attributes; the target can feature multiple values of Gaussian curvature in response to a given temperature change that can be either uniformly or locally applied. Fig. 1 illustrates the overall scope of our morphing platform through an illustrative example. In Fig. 1a, a flat multimaterial spatial lattice (only upper surface shown) is programmed at the initial temperature (T_0) with a target curvature field to reconfigure into a target shape (Fig. 1b) in response to uniform heating to T_1 ($T_1 > T_0$). In addition, the design space of existing concepts is here extended by modulating the applied stimulus locally and in reverse, the former reported merely only for self-folding [43,44], and the latter, i.e., stimulus reversal rarely documented in bending and buckling strategies. By combining heating or cooling, either globally or locally, we demonstrate inverse morphing (Polymorphing I) and localized morphing (Polymorphing II). The former (Fig. 1c) is obtained through a uniform switch of temperature from heating to cooling ($T_2 < T_0$), a stimulus inversion yielding a curvature reversal in the target shape; the latter (Fig. 1d) leverages a local thermal exposure to morph the truss in individual regions. Finally, the stimulus removal with temperature returning to T_0 (Fig. 1d-a) enacts fully reversible morphing, where truss morphing reverts to the initially unmorphed state due to the passive nature of the truss constituents.

2. Results

This section first presents a single unit cell and explains its temperature-responsive mechanism of spatial deformation, followed by a description of their ensemble into homogeneous and heterogeneous truss metamaterials attaining global transformations. We then describe a scheme to achieve structural morphing on target that is experimentally validated on proof-of-concept prototypes.

¹ Coefficient of thermal expansion

2.1. Mechanisms of a temperature-responsive unit cell

We start with a cuboid, truss-like unit cell composed of four facets. Each facet consists of individual trusses arranged in an axisymmetric pattern with opposite facets featuring identical material and geometry (Fig. 2a, left). The trusses are grouped into two sets, the core and frame, composed of passive, thermally responsive solids that spatially interact to enable temperature-induced deformations. In particular, upon an increase in temperature, the unit cell deforms through the volumetric expansion of the trusses induced by the CTE mismatch between the core and the frame.

To capture the effect of the CTE mismatch between the frame and core on the temperature-responsive deformation of our 3D unit cell, we first focus on a single facet (Fig. 2a, inset) that we model as a pin-jointed planar framework (Supplementary Note 1 and Supplementary Fig. 1). The insights gained from this first analysis will ease the understanding of the spatial behavior of our 3D multimaterial truss. To do so an individual facet is pinned along a frame edge, and the displacement of joints \mathbf{d} can be determined from the temperature-induced elongation \mathbf{e} of each truss member, which can be calculated through the analysis of the kinematic matrix \mathbf{B} of the truss (Supplementary Note 1.2):

$$\mathbf{B} \cdot \mathbf{d} = \mathbf{e} \quad (1)$$

where \mathbf{B} is a 7×7 matrix, equal to the transpose of its equilibrium matrix, for the pin-jointed facet framework. The temperature-induced elongation, \mathbf{e} , can be expanded by the product of the change in temperature, ΔT , CTE for each truss, and the initial truss length \mathbf{s} (Supplementary Fig. 1a):

$$\mathbf{e} = \Delta T \cdot \text{CTE} \cdot \mathbf{s} = \Delta T \begin{bmatrix} \alpha_1 & 0 & 0 & 0 & 0 & 0 & 0 \\ 0 & \alpha_2 & 0 & 0 & 0 & 0 & 0 \\ 0 & 0 & \alpha_3 & 0 & 0 & 0 & 0 \\ 0 & 0 & 0 & \alpha_4 & 0 & 0 & 0 \\ 0 & 0 & 0 & 0 & \alpha_5 & 0 & 0 \\ 0 & 0 & 0 & 0 & 0 & \alpha_6 & 0 \\ 0 & 0 & 0 & 0 & 0 & 0 & \alpha_7 \end{bmatrix} \begin{bmatrix} s_1 \\ s_2 \\ s_3 \\ s_4 \\ s_5 \\ s_6 \\ s_7 \end{bmatrix} \quad (2)$$

We then apply the following constraints imposed by the material and geometry of the trusses in the facet as:

$$\alpha_1 = \alpha_2 = \alpha_7 = \alpha_f, \quad \alpha_3 = \alpha_4 = \alpha_5 = \alpha_6 = \alpha_c \quad (3)$$

$$s_2 = \frac{s_1}{2} (\tan \theta_1 + \cot \theta_2), \quad s_3 = \frac{s_1}{2 \sin \theta_2}, \quad s_4 = \frac{s_1}{2 \cos \theta_1}, \quad s_5 = s_4, \quad s_6 = s_3, \quad s_7 = s_2 \quad (4)$$

where α_c and α_f denote the CTEs of the core and frame. The deformation of the facet herein is described by the curvature and displacement, the former assessing the deformation amplitude of a curve that deviates from a straight line, and the latter denoting the direction of curvature. Curvature, k , is defined as the reciprocal of the radius of the circle whose center is the intersection point of the extensions of two initially parallel frame trusses that rotate due to the thermal stimulus, and the radius is the distance from the center to edge of the horizontal frame truss (Fig. 2a, right and Supplementary Fig. 1b). The direction of curvature, defined by the displacement component d_2 , is measured as a shift from the initial location of the horizontal frame truss under a temperature change of ΔT . This shift can be expressed by the relation:

$$\frac{d_2}{\Delta T} = l_1 (\alpha_c - \alpha_f) \left(\frac{1}{\frac{2l_3}{l_1} - \tan \theta} + \tan \theta \right) \quad (5)$$

where θ , l_1 , and l_3 are the skew angle and lengths, respectively, of the horizontal and vertical truss of the facet shown in Fig. 2a, left, and have the relationships $l_1 = s_1$, $l_3 = s_2$, $\tan \theta = 2l_3 /$

$l_1 - \tan \theta_1 = \cot \theta_2$. For a given temperature change and combination of CTEs for the frame (α_f) and core (α_c), we can characterize the global deformation of the facet through the curvature and displacement, as defined above. For example, if $\alpha_f = \alpha_c$, no mismatch in CTE exists, and thus no change in curvature can be observed upon heating ($k = 0$). On the other hand, if $\alpha_f > \alpha_c$, the core volumetrically expands more than the frame resulting in a positive curvature ($k > 0$). Alternatively, the frame endowed with greater volumetric expansion than the core, i.e., $\alpha_f < \alpha_c$, leads to a negative curvature ($k < 0$) (Supplementary Fig. 1b). In addition to the CTE, the axial elastic modulus of the core and frame trusses (E_c , E_f) contributes to the deformation of the rigid-jointed facet. This suggests that we can quantitatively map the role of the pair of material attributes (E_c / E_f and $\alpha_c - \alpha_f$) in the material property space of a facet as shown in Fig. 2a. The constituent materials are assumed to remain in the elastic regime during thermal deformation. This map depicts the control exerted by the material properties on the deformation mode and the spectrum of curvature values that can be attained for a given architecture of the truss facet. A curvature distribution with a remarkable range from $-4.5 \times 10^{-3} \text{ mm}^{-1}$ to $7.2 \times 10^{-3} \text{ mm}^{-1}$ can be attained by harnessing materials with a large distinction in CTE.

Expanding from an individual facet, we begin to explore the deformation our 3D unit cell with prescribed topology can attain for alternative arrangements of materials and geometric parameters. We first select two points in the material property space (Fig. 2a, right), A ($\alpha_c - \alpha_f = -5.58 \times 10^{-5} \text{ K}^{-1}$, $E_c / E_f = 51.7$) and B ($\alpha_c - \alpha_f = 8.4 \times 10^{-5} \text{ K}^{-1}$, $E_c / E_f = 1.409$), each describing a deformed state with either negative or positive curvature, respectively. Assigning a given material arrangement, i.e., point A or/and B, at each facet, yields distinct global deformation at the level of the unit cell. Three representative choices are examined for demonstrative purposes: unit cell A-A (Fig. 2b, left), B-B (Fig. 2c, left) and A-B (Fig. 2d, left), each capable of expressing an individual mode of deformation upon heating. In particular, a unit cell composed of either material A or B, i.e., A-A or B-B unit cell, displays either negative or positive curvatures, k_1 and k_2 , upon an increase in temperature, whereas one allocated with both materials A and B, i.e., A-B unit cell, shows concurrently negative (k_1) and positive (k_2) curvature.

The results above demonstrate that the material composition of each facet and their arrangement govern the global deformation mode of the unit cell. The geometric attributes, on the other hand, control the magnitude of the response, and are now examined. Among the geometric parameters defining our unit cell, we focus here on the skew angles θ and γ , since their role most influences the unit cell response for a given temperature change of 120°C ; other geometric parameters are prescribed at the following values: $l_1 = l_2 = 19 \text{ mm}$; $l_3 = 50 \text{ mm}$; $t_0 = 1 \text{ mm}$; $t_c = 0.5 \text{ mm}$, material A; $t_c = 0.8 \text{ mm}$, material B. The role of θ and γ is mapped in the geometry spaces visualized in Fig. 2b-d. Here the map shows the attainable ranges of curvatures k_1 , k_2 the unit cell A-A, B-B, and A-B can attain by tuning θ and γ within prescribed ranges. As the A-A and B-B unit cells consist of one single material (A or B) and are mapped within the identical spectrum of skew angles θ and γ , the resulting curvature distributions k_1 and k_2 do not differ, and the curvature distribution is displayed as a single profile k_2 ; this result applies to k_1 as well when switching the coordinates of θ and γ . As for the A-B unit cell, comprising both material A and B, two deformation profiles k_1 and k_2 emerge, and two surface responses are provided to assess the achievable values of curvatures that are opposite in sign.

The trends in Fig. 2 show that the larger the skew angle for a given facet, the more sizeable its response. Programming the unit cell geometry, in this case through tuning θ and γ , enables to induce a sizable deformation for a given pair of materials. For exam-

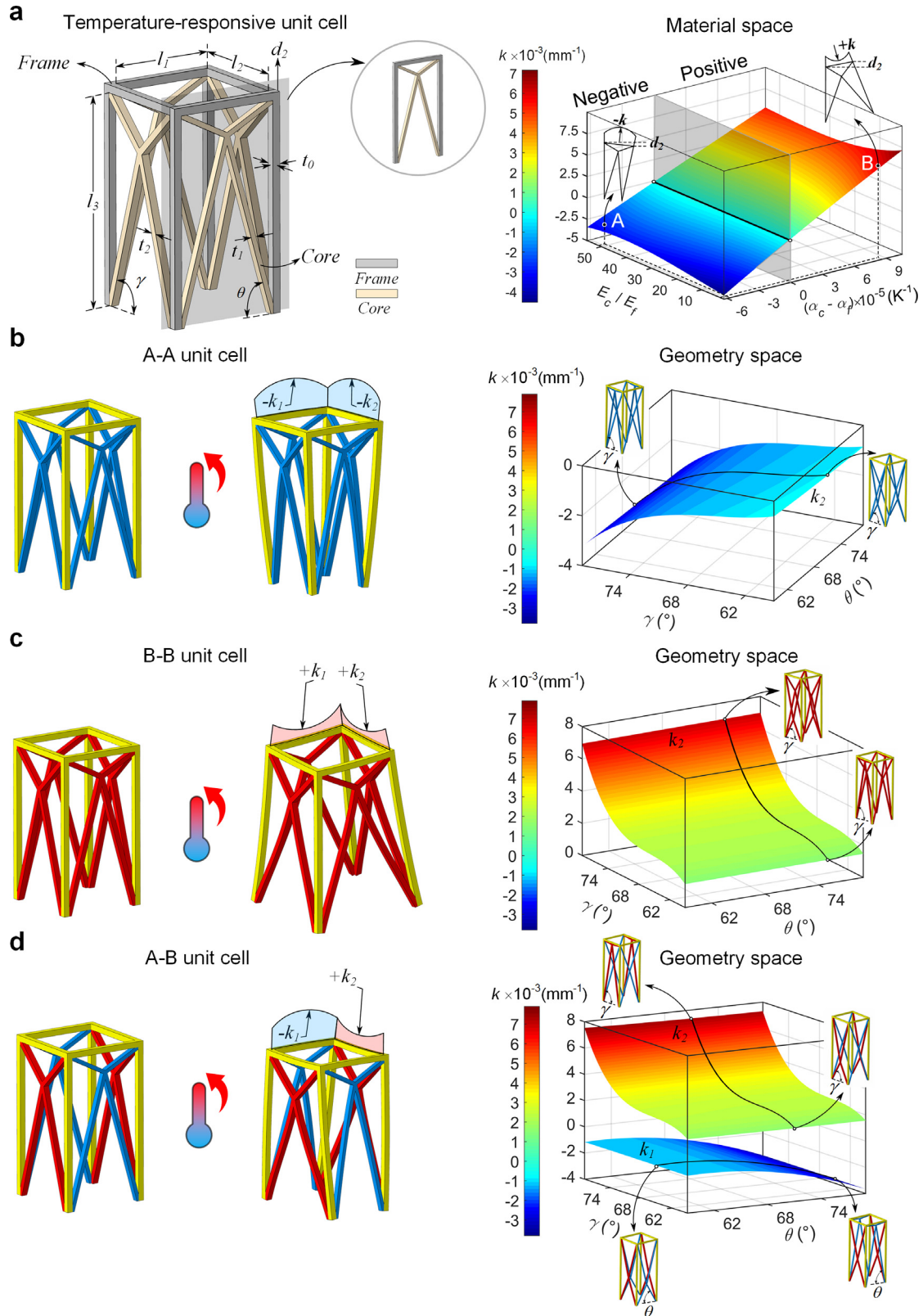


Fig. 2. Truss architecture of thermally responsive unit cell and attainable curvatures for given material arrangement. **a, left** Unit cell composed of four facets with the opposite ones characterized by identical material and geometry. Each facet is composed of trusses that consist of two distinct temperature-responsive materials, labeled either the core or frame, and arranged in an axisymmetric pattern. **a, right** Achievable range of curvature, k , for an individual facet measured in the material space ($\alpha_c - \alpha_f$ versus E_c / E_f ; f : frame, c : core) for given temperature change of 120°C with prescribed dimensions $l_1 = 19\text{ mm}$, $l_3 = 50\text{ mm}$, $t_0 = 1\text{ mm}$, $t_1 = 0.5\text{ mm}$ and $\theta = 74^\circ$. The unit cells consist of materials with properties identified by the coordinates of point, A ($-k$: $\alpha_c - \alpha_f = -5.58 \times 10^{-5}\text{ K}^{-1}$, $E_c / E_f = 51.7$) and B ($+k$: $\alpha_c - \alpha_f = 8.4 \times 10^{-5}\text{ K}^{-1}$, $E_c / E_f = 1.409$). **b-d, left** Unit cell A-A, B-B, and A-B, each with its own material arrangement and distinct response to an increase in temperature. Truss bending deformation amplified for visual purpose. **b-d, right** Resulting curvature profiles spanned by skew angles θ and γ within defined ranges, with other dimensions prescribed: (b) $l_1 = l_2 = 19\text{ mm}$, $l_3 = 50\text{ mm}$, $t_0 = 1\text{ mm}$, $t_1 = t_2 = 0.5\text{ mm}$ (c) $l_1 = l_2 = 19\text{ mm}$, $l_3 = 50\text{ mm}$, $t_0 = 1\text{ mm}$, $t_1 = t_2 = 0.8\text{ mm}$ (d) $l_1 = l_2 = 19\text{ mm}$, $l_3 = 50\text{ mm}$, $t_0 = 1\text{ mm}$, $t_1 = 0.5\text{ mm}$, $t_2 = 0.8\text{ mm}$. Insets depict unit cell with changes in angle θ (γ) at a given γ (θ) along continuous curves. By varying the skew angle from 59° to 79° , the absolute values of curvature increase by: (b) 286.4% in k_2 (k_1) at $\theta(\gamma) = 71^\circ$, (c) 335.3% in k_2 (k_1) at $\theta(\gamma) = 75^\circ$, (d) 290% in k_1 at $\gamma = 65^\circ$ and 333.3% in k_2 at $\theta = 71^\circ$.

ple, by varying γ (θ) from 59° to 79° the absolute change in k_2 (k_1) is 286.4% at θ (γ) = 71° for the unit cell A-A (Fig. 2b), and 335.3% at θ (γ) = 75° for the unit cell B-B (Fig. 2c). On the other hand, an increment of θ from 59° to 79° generates an absolute change of 290% in k_1 at $\gamma = 65^\circ$ and an identical increase of γ results in a 333.3% gain in k_2 at $\theta = 71^\circ$ for the unit cell A-B (Fig. 2d). In addition to the skew angles θ and γ , other geometric parameters, such as the frame length ratio l_1 / l_3 , l_2 / l_3 , the core-frame thickness ratio t_1 / t_0 , t_2 / t_0 and the frame thickness t_0 , can be tuned but the results show a narrow capacity for cell response tailoring (Supplementary Note 2 and Supplementary Fig. 2).

2.2. Encoded ensembles of unit cells for thermally responsive truss metasurfaces

We now expand upon the unit cell and showcase how their ensemble can act collectively as an integral lattice to create a rich set of global shape transformations. The Gaussian curvature, K , is introduced to characterize the surfaces generated from an initially flat plane representing the joined upper faces of the lattice. The unit cell assembly can be varied by manipulating its core/frame material composition, geometry, or periodicity, resulting in distinct deformed surfaces featuring either positive ($K > 0$), neutral ($K = 0$), or negative ($K < 0$) Gaussian curvature. Here, we first examine homogenous trusses of uniform tessellations featuring one single type of unit cell, and then in the next section illustrate the potential of combining dissimilar unit cells for shape morphing on target.

As an illustrative example, to achieve a global geometry with positive K such as a spherical lattice, Fig. 3a, left shows that it is sufficient to tessellate a single B-B into a square lattice; whereas to obtain a global geometry with negative K , such as a saddle lattice, we can switch the type B-B unit to the A-B unit cell, and tessellate the latter again in the squared pattern (Fig. 3a, right).

Other transformations can also be obtained by manipulating the lattice tessellation and material composition. For example, two distinct morphed shapes, cylindrical helix ($K = 0$) and twisted helix ($K < 0$), can be obtained by assigning dissimilar materials to the cores of constitutive unit cells that are tessellated in an inclined ribbon pattern. In particular, a cylindrical-helix lattice featuring zero Gaussian curvature K necessitates the introduction of anisotropic curvatures with one zero ($k_1 = 0$) and the other nonzero ($k_2 > 0$) along perpendicular directions. This can be realized if the unit cells are allocated with material B and another pair, where the frame and core share a given material (Fig. 3b, left). On the other hand, to achieve a twisted helical shape with negative Gaussian curvature K , the use of A-B unit cells can simultaneously generate positive and negative curvatures (Fig. 3b, right).

While the above homogeneous lattice design can accomplish a variety of global transformations from an initially flat configuration, heterogeneous lattices with skew angle gradients can be programmed to expand the geometric diversity of the attainable morphing shapes. For example in Fig. 3c, the lattice is divided into two segments with the skew angle of the unit cells $\gamma_1 = 65.2^\circ$ on the left and $\gamma_2 = 69.9^\circ$ on the right, and the material arrangement, as well as other geometries, are identical across the rectangular lattice. The results show that distinct magnitudes of curvature can be introduced within the ribbon upon heating, yielding a double-spiral shape (Fig. 3c).

2.3. Morphing on target via encoded unit cells

So far, we have created a variety of metasurfaces with either positive, zero, or negative constant values of Gaussian curvature, as well as curvature gradients using homogenous and heterogeneous aggregates of unit cells. Here, we take a step forward and

demonstrate how to obtain morphing-on-target shapes of broader geometric diversity, allowing for multiple Gaussian curvature values to be concurrently encoded into a single lattice.

The strategy that we pursue here is to program the global response to temperature through the local tuning of each unit cell response, thus generating a lattice ensemble that collectively morphs into a predefined shape. To demonstrate this route, we first consider a generic target surface with varying curvatures that is generated by extruding one curve, C_p , along another, C_v (Fig. 4a). The surface is then discretized, resulting in a 21×22 target surface mesh with equidistant spacing l along X and Y direction in our surface (Fig. 4b). Through this discretization, the curves on the surface can be closely approximated by the aggregation of straight-line segments between adjacent vertices (Supplementary Fig. 3b). We then extract the 3D coordinates of each vertex on the mesh and compute the curvature values at each vertex. Each value of curvature is averaged along each line segment, and the full curvature field is then mapped to the target surface mesh (Fig. 4b).

The target surface mesh is subsequently flattened onto the X-Y plane and the coordinates (x , y) of each vertex are calculated. As the curve C_p locates in the X-Z plane, the flattened curve C_p is superimposed on the X axis, causing the y coordinates of the vertices on it to equal zero, i.e., $P'_i(x'_{p_i}, 0)$. Similarly, the x coordinates of the vertices on the flattened curve C_v overlaid on the y axis equal zero, i.e., $V'_j(0, y'_{v_j})$. The missing components of the (x , y) coordinates of the points on the flattened curve C_p and C_v can then be obtained by superimposing on the corresponding zero coordinates the lengths of line segments connecting neighboring points, which can be mathematically expressed as:

$$x'_{p_i} = \sum_{m=1}^{i-1} \| \mathbf{p}_{m+1} - \mathbf{p}_m \| \quad i = 2, \dots, 22 \quad (6)$$

$$y'_{v_j} = \sum_{n=1}^{j-1} \| \mathbf{v}_{n+1} - \mathbf{v}_n \| \quad j = 2, \dots, 23 \quad (7)$$

where $\| \mathbf{p}_{m+1} - \mathbf{p}_m \|$ denotes the distance between the point P_m and P_{m+1} ($m = 1, 2, \dots, 21$) along C_p and $\| \mathbf{v}_{n+1} - \mathbf{v}_n \|$ represents the distance between the point V_n and V_{n+1} ($n = 1, 2, \dots, 22$) along C_v (Supplementary Fig. 4). By this means, we can obtain the planar coordinates of any given point $G'_{i,j}(x'_{g_i}, y'_{g_j})$ in the X-Y plane that is associated with $G_{i,j}$ in space:

$$x'_{g_i} = \sum_{m=1}^{i-1} \| \mathbf{g}_{m+1,j} - \mathbf{g}_{m,j} \| \quad i = 2, \dots, 22 \quad (8)$$

$$y'_{g_j} = \sum_{n=1}^{j-1} \| \mathbf{g}_{i,n+1} - \mathbf{g}_{i,n} \| \quad j = 2, \dots, 23 \quad (9)$$

where $\| \mathbf{g}_{m+1,j} - \mathbf{g}_{m,j} \|$ measures the distance between the adjacent points along the X direction starting from the point V_j , while $\| \mathbf{g}_{i,n+1} - \mathbf{g}_{i,n} \|$ calculates the length of the line segment along the Y direction originating from the point P_i . Once we access the complete information of the flattened mesh in the X-Y plane, the previously computed curvature field is mapped to the flattened mesh as well (Fig. 4b). During the flattening process, we assume a linear in-plane growth owing to a thermal expansion value that is negligible compared to the original lattice dimension as its amplitude for a temperature change of 120°C is limited to the order of 10^{-2} .

The next step involves encoding the geometric and material information of the unit cells to match the curvature field of the target surface. We prescribe the length and thickness of our unit cells, and then determine their material and geometric attributes capable of matching the target curvature of the discretized surface. As the control over two curvatures k_1 and k_2 of a unit cell via the skew angles θ and γ is coupled, minute differences appear in the calculated values of θ s and γ s for unit cells along y and x, respectively. To connect those units with minor variations in θ or

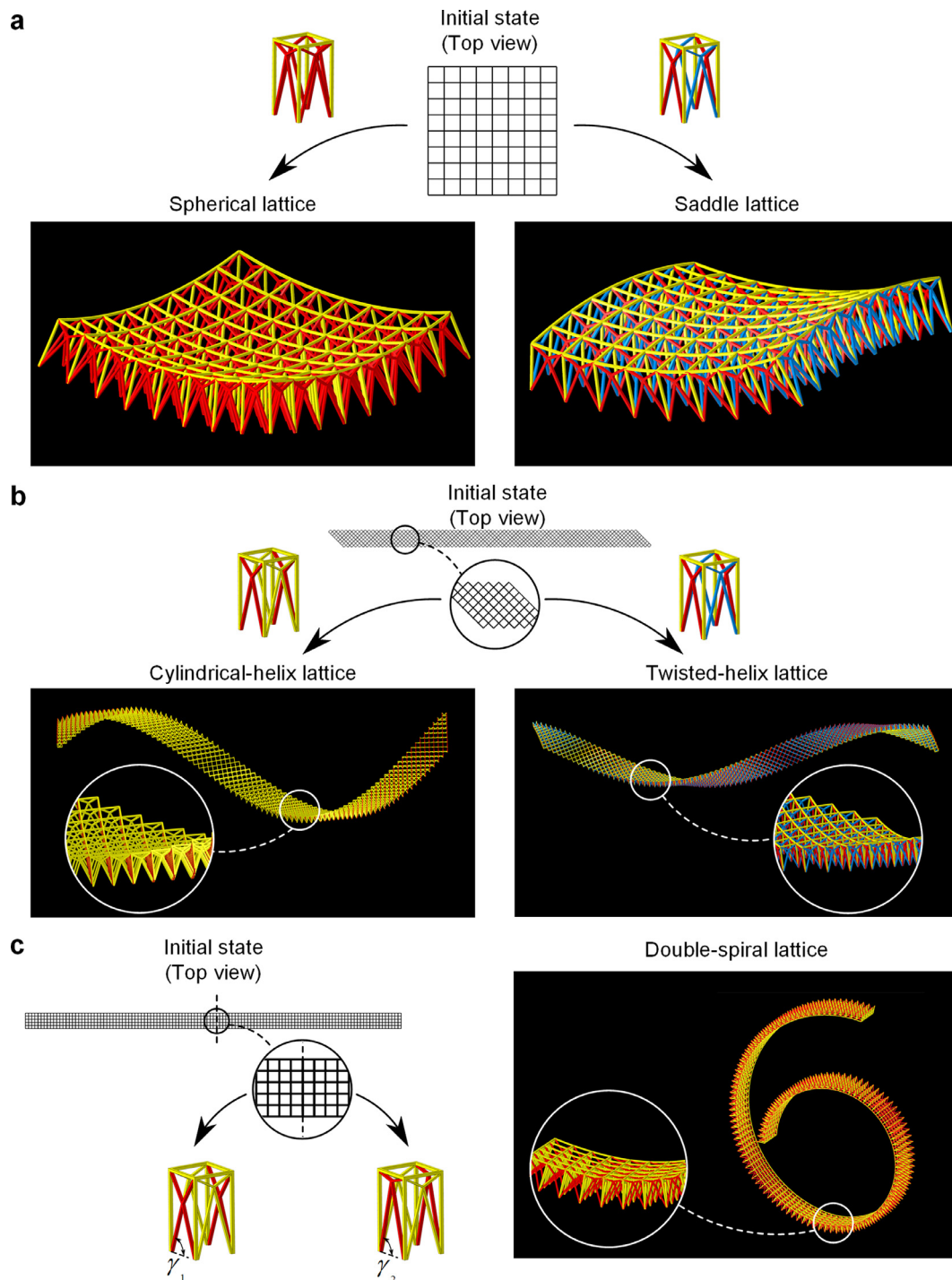


Fig. 3. A wide variety of morphologies emerging upon uniform heating from alternative aggregates of unit cells. Initial configurations and deformed lattices are depicted in subplots from top to bottom **a**, top Square lattice composed of B-B (left) and A-B (right) unit cells, respectively, in undeformed state. **a**, bottom Spherical ($K > 0$) and saddle ($K < 0$) shape attained from the initially flat lattice after applying a temperature change of 120 °C. Insets show close-up of the lattice. **b**, top Inclined narrow stack of unit cells in undeformed state. In the left representative unit cell, material B is assigned to two opposite facets and another pair, where the frame and core share the same material, is assigned to the others, whereas the right representative unit cell consists of material A. **b**, bottom Cylindrical helix ($K = 0$) and twisted helix ($K < 0$) transformed from a narrow ribbon shape, upon a temperature change of 120 °C. Insets show close-up of the lattice. **c**, left Rectangular lattice comprising unit cells with skew angle gradients, i.e., $\gamma_1 = 65.2^\circ$ on the left segment, and $\gamma_2 = 69.9^\circ$ on the right. **c**, right Double spiral formed under an applied temperature change by introducing in the lattice curvature gradients derived from the disparity of the skew angle γ . Insets show close-up of the lattice.

γ , the weighted average value of the skew angle is evaluated and assigned to the unit cells. Finally, the unit cells embedded with programmed material and geometry are assembled into a truss-lattice surface (Fig. 4c) that is capable of reconfiguring into the target shape when heated to a prescribed temperature (Fig. 4d–e).

To assess the agreement between the deformed lattice and target surface, we extract the point cloud of the deformed lattice that contains the 3D coordinates of the midpoint on the top surface of each vertical frame truss and align it with the target 3D triangle mesh of the target surface. The nearest neighbor distance be-

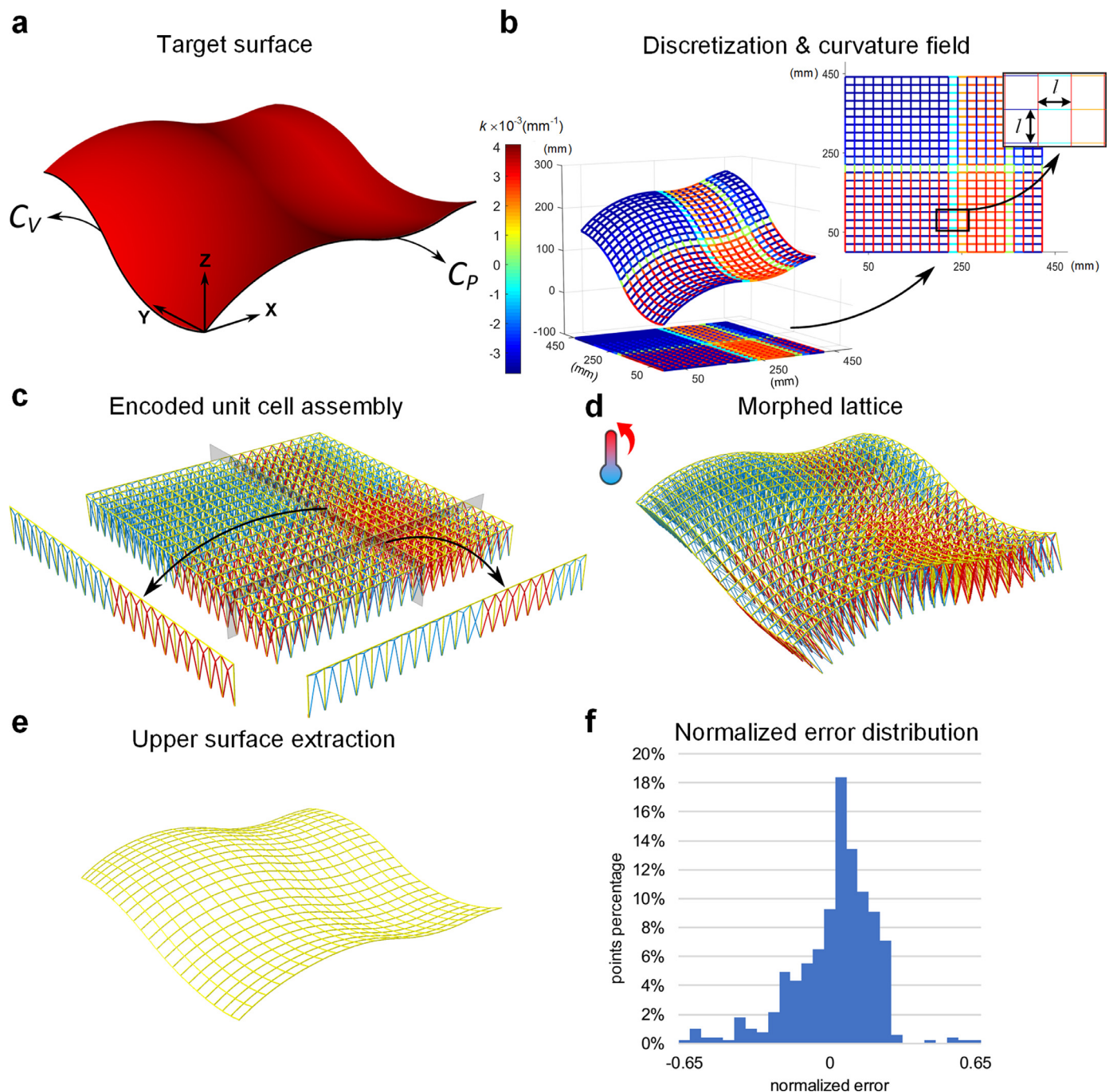


Fig. 4. Demonstration of 3D shape morphing on target attained by an encoded ensemble of unit cells with locally programmed curvature. **a** Representative target surface. **b** Discretized and flattened target surface with equidistant grid spacing l mapped with the target curvature field k . **c** Assembly of unit cells encoded with target curvatures through programmed material and geometry attributes. Inset depicts illustrative encoded facets in perpendicular planes. **d** Morphed configuration of the initially flat lattice under a temperature change of 120 °C. **e** Upper surface extraction of the morphed lattice. **f** Normalized error distribution derived from the distance between the retrieved point cloud of the deformed lattice and the target 3D triangle mesh; 96.2% of points lie in the normalized error range: -0.5 to 0.5 . A point with positive error locates above the target mesh whereas a point with negative error lies beneath the target mesh.

tween each point in the lattice point cloud and the target mesh is calculated and normalized. The resulting distribution of the normalized error shows good agreement with 96.2% of the points falling in the range of ± 0.5 (Fig. 4f). The inverse design procedure and error analysis are explained in more detail in Supplementary Note 3.

2.4. Experimental validation

We now provide a qualitative proof of the types of curvature and combination thereof we can achieve. We manufactured multi-

material samples and tested their shape morphing behavior. Thermal tests were carried out in a heating chamber with temperature ranging between 25 and 75 °C. Fig. 5 and Supplementary Movie 1 show the results. Upon heating, a saddle shape, a twisted helix, both with negative Gaussian curvature K , and a cylindrical helix with zero K are generated from the flat lattices constructed of unit cells arranged in a 5×5 square, 5×15 parallelogram, and 4×9 parallelogram configuration, respectively (Fig. 5a–c). These three lattices employ the same unit cell type and tessellation pattern as those illustrated in Fig. 3a, right and Fig. 3b, and show consistent deforming tendency upon heating. Next, Fig. 5d shows a represen-

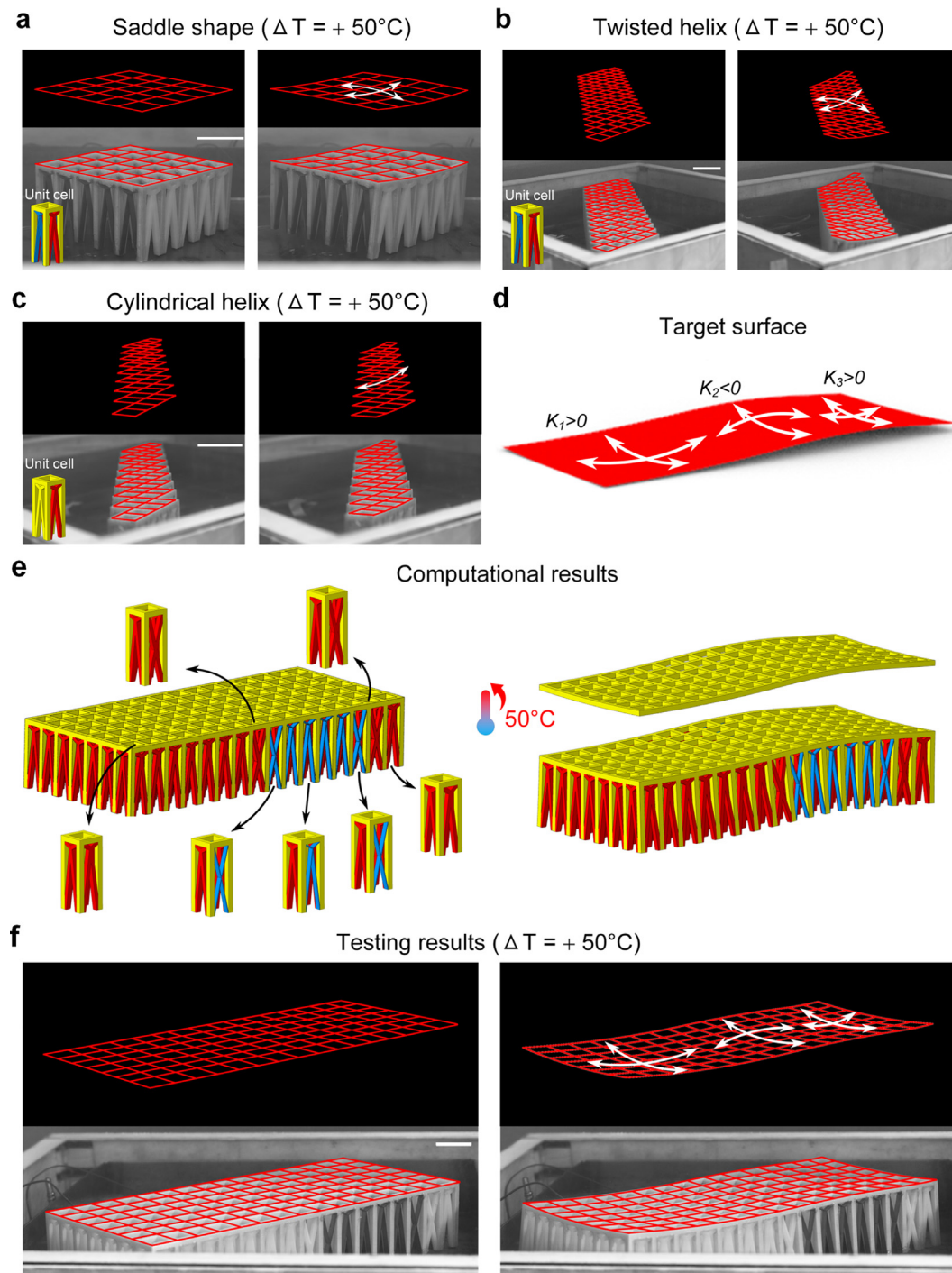


Fig. 5. Multiple metasurfaces of reversible shape morphing achieved through fabricated prototypes under heating. Insets show the material arrangement of unit cell for each lattice. a–c Saddle shape ($K < 0$), twisted ($K < 0$) and cylindrical helix ($K = 0$) formed, respectively, from initially flat lattices comprising multiple materials under a temperature increase of 50°C . **d–f** Representative target surface, computationally calculated and experimentally observed results obtained through a programmed lattice when the prescribed temperature change of 50°C is reached. Scale bars = 26 mm . The left-hand side of images of (a), (b), (c), and (f) show configurations both prior and post application of the thermal stimulus, hence demonstrating reversible shape morphing.

tative target surface chosen for the experimental validation of our morphing on target. The demonstrative surface displays three regions with Gaussian curvatures $K_1 > 0$, $K_2 < 0$, and $K_3 > 0$, respectively. The specimen consists of 7×16 unit cells with their encoded material and geometric attributes, assembled in a rectangular configuration (Fig. 5e). The experimental results (Fig. 5f) demonstrate that the upper surface of the encoded truss system can generate both the positive and negative Gaussian values of curvature of the target surface upon an applied temperature range of 50°C .

3. Discussion

Aside from the typical square unit cell, alternative unit cell shapes, such as triangles, parallelograms, and hexagons, can be constructed by arranging the facets in various ways. A lattice ensemble can then be created by tessellating not only one type of unit cell, in this case a square unit, but a combination of units of distinct shapes. As a result, the encoded lattices are not confined to a square layout, expanding the design space for target surfaces.

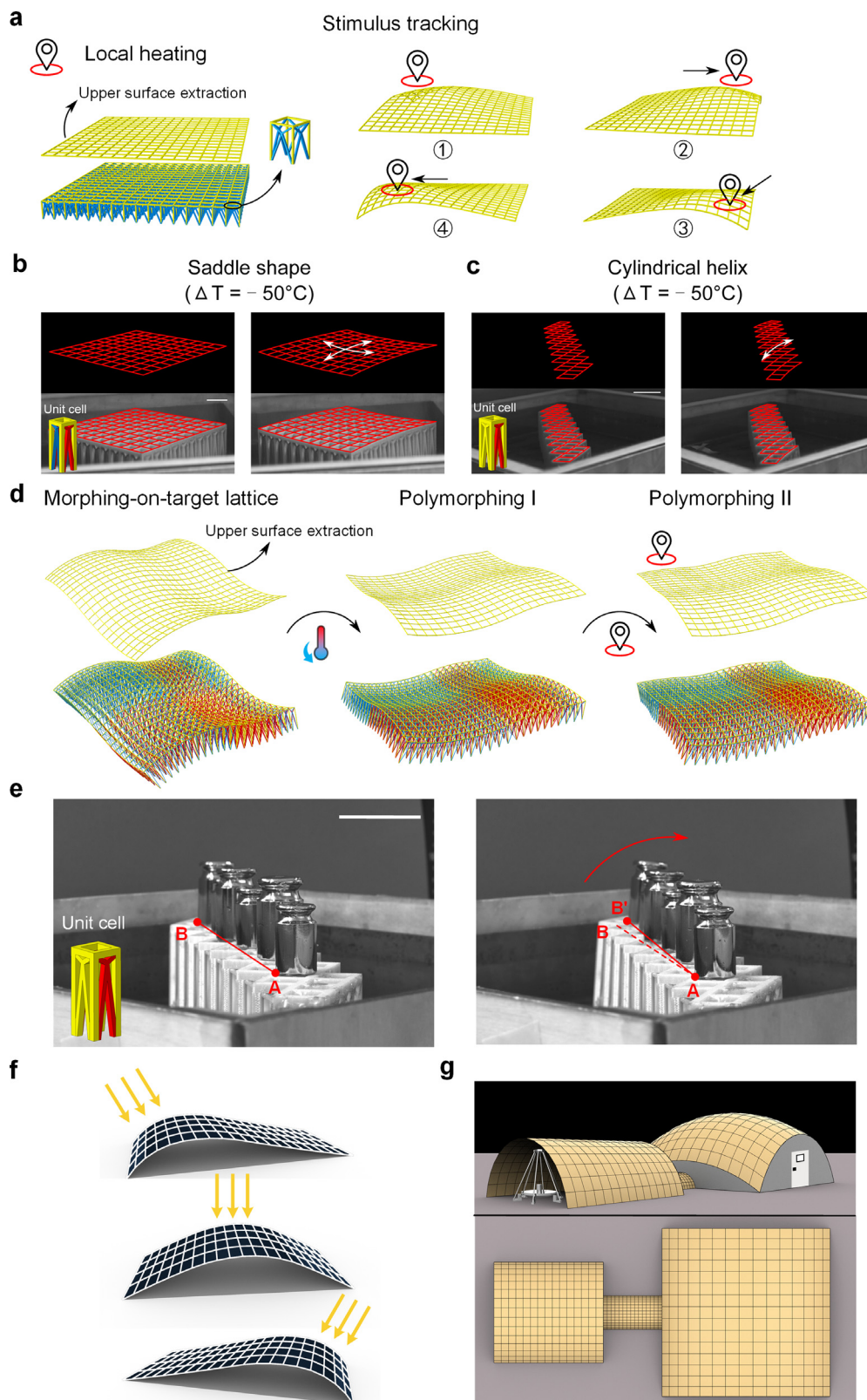


Fig. 6. Localized and inverted lattice deformation through local heating and cooling, load bearing capacity and potential applications. **a** Stimulus tracking behavior achieved by locally heating the multimaterial truss. A flat lattice made up of A-A unit cells bumps up at a specific location upon local heating. The protrusion of the lattice tracks the thermal stimulus, here applied clockwise for demonstrative purposes (①→②→③→④), resulting in a heat source tracking behavior. **b** Lattice featuring identical material arrangement deforming into a saddle shape with opposite curvature directions when switching heating to cooling. Scale bars = 26 mm. **c** Cylindrical helix transformed from a lattice comprising two materials arranged in a narrow ribbon shape upon cooling. Scale bars = 26 mm. **d** Sequential transformations of the programmed lattice obtained from a cycle of cooling and local heating. When the stimulus shifts from heating to cooling, the morphing-on-target lattice undergoes inverse deformation (Polymorphing I). Next, a dented area bumps up when this region experiences an increase in temperature, leading to a distinct shape (Polymorphing II). **e** Load bearing capacity of the cylindrical-helix lattice in both its undeformed and deformed states. Scale bars = 26 mm. **f** Compliant solar array transforming with the changing position of the heat source without onboard electronics. **g** Space shelter for explorers and equipment. The left-hand side of images of (b), (c), and (e) show configurations both prior and post application of the thermal stimulus, hence demonstrating reversible shape morphing.

As opposed to programming the internal attributes of a construct, i.e., its material and geometric properties, to obtain manifold shape morphing, the external stimuli, in this case temperature, can be also modified to explore the morphing evolutions over time. Current strategies have typically achieved self-folding via locally applied stimulus [43,44]. In this work, we demonstrate inverse and localized deformation by applying external activation in local and reverse manner. Specifically, localized deformation has been introduced through local application of a thermal source, in addition to the uniformly applied heating yielding global lattice transformation. For example, a lattice made up of A-A unit cells ($k_1, k_2 < 0$), which morphs into a spherical shape under uniform heating, can be locally deformed by selectively heating the lattice at a given location (Fig. 6a). Here for demonstrative purpose, the thermal stimulus is applied starting from the back left corner and rotating clockwise (①→②→③→④), resulting in stimulus tracking, a behavior where the protrusion of the lattice follows the heat source.

The rich set of 3D geometries so far presented have been realized under heating; however, further shape morphing can be introduced with a stimulus reversal. Specifically, we demonstrated that when the stimulus switches from heating to cooling, the lattices can exhibit inverse curvature values under the assumption that the material properties are unvarying. This inverse deformation arises from the inverse relationship of the volumetric change between the constituent materials when the stimulus shifts from heating to cooling. A set of experiments were conducted to validate this. When switching the stimulus from heating to cooling, a flat 10×10 square lattice (Fig. 6b), which has the material arrangement of that in Fig. 3a, right, and Fig. 5a, deforms into a saddle shape as well, but its deformed curvatures are in the opposite direction. Similarly, a bi-material narrow strip specimen (Fig. 6c), composed of 4×9 unit cells and characterized with the material pattern shown in Fig. 3b, left, forms a cylindrical helix that curves in the opposite direction due to the shift from heating to cooling.

By combining heating or cooling, either globally or locally, the design space of our spatial multimaterial lattices can be expanded to achieve polymorphing. As an illustrative example, the target lattice discussed in Fig. 4 obtained by heating the encoded flat lattice to a prescribed temperature (Fig. 6d, left; Supplementary Movie 2), is cooled down below the original temperature to transform into Polymorphing I, an inverse transformation of the lattice (Fig. 6d, middle; Supplementary Movie 2). Next, by superimposing local heating at a specific spot, the curvature values are inverted in the region that was previously dented, resulting in Polymorphing II (Fig. 6d, right; Supplementary Movie 2).

In addition to the morphing characteristics, we show the load bearing capacity of the lattices through a set of experiments (Fig. 6e), where the lattice specimen (190.5 g) presented in Fig. 6c is capable of carrying 450 g weight, nearly 2.4 times its own weight, in both its undeformed and deformed states. More details on the demonstration of load bearing ability are available in Supplementary Note 4 and Supplementary Fig. 6.

We envision our multimaterial truss design could be applied in a range of applications, including space-faring scenarios, where environmental temperature variations are significant and readily available. For example, to provide sufficient energy for space exploration and immigration, the local temperature-responsive feature of our lattices could be integrated into a compliant solar energy system. In the case of a nonuniform temperature distribution caused by changes in the angle of solar radiation across a massive solar array, the solar panels can track the heat source without needing additional sensors or motors (Fig. 6f). The experimental validation of the localized deformation is included in Supplementary Note 5 and Supplementary Fig. 7. Our multimaterial truss could also function as a temporary shelter or cover for explorers and delicate equipment on exoplanets that only appear under

a given temperature fluctuation (Fig. 6g). Other potential applications include a space-based optical mirror that can adjust reflection direction of light or signal without onboard actuators by virtue of surface deformation over a temperature variation. Because of the initially flat configuration, substantial room can be saved during launch or for storage. These packed appliances can in turn reconfigure into desired 3D structures that meet specific design requirements by leveraging extraterrestrial environment temperatures.

In addition to the positive temperature changes, negative variations in temperature are another scenario in outer space due to day-night shift. Space instruments typically are designed to work during the day and get into sleep mode at night. However, with the capability of multiple morphologies through a single lattice in response to both positive and negative temperature changes, these instruments that rely on the lattice deformation by leveraging predictable temperature fluctuations can work not only during the day but also at night.

Another reason our framework has promising practical applications is its capacity to transform into distinct shapes without having to modify the entire construct, which may benefit savings in materials and manufacturing time, particularly in engineering applications where resources are very limited and valuable. As an illustrative example in Fig. 3a, by replacing half of the red cores ($k_1 > 0$) with the blue ones that feature dissimilar characteristic ($k_1 < 0$) while keeping the frame unaltered, the lattice that was designed to display spherical shape alternatively turns into a saddle shape under the same stimulus.

4. Conclusions

The ability to generate complex 3D truss surfaces from an initially flat configuration can open a unique paradigm for structural shape morphing that can find applications in a broad range of engineering sectors. In this work, we have introduced a 3D truss concept for the unit cell that differs from existing thin layered structures [31,41,45] and can employ passive materials, resulting in stiff and lightweight structural architecture with morphing reversibility. We have showcased how the unit can be tuned across a range of geometric and material features; with the achievable ranges of curvature, the encoded ensembles of unit cells enable a rich set of morphologies in response to a temperature stimulus. More complex predefined surfaces with multiple Gaussian curvatures can be achieved by encoding a target curvature field into the aggregate of unit cells when the prescribed temperature change is reached.

Our platform can be broadened to other materials and stimuli, provided that the input source would induce a mismatch in volumetric change between the constituent solids. The ability of 3D shape programming and polymorphic transformations could accommodate a large range of application scenarios, where the variations in external stimuli are accessible. The fabrication method is not limited to multimaterial 3D printing, as the frames and cores can be manufactured separately and then joined on mission site using current structural engineering techniques for truss assembly. The size of unit cell can also be scaled up to create a large, structure-efficient truss system that can carry its own weight and cover a large area. Moreover, in this work we employ passive materials to attain reversible shape morphing as opposed to active materials, whose use typically requires a tight intertwine between chemical recipes and tuned process of fabrication, such as PolyJet and HP Multi Jet Fusion. Shape morphing using active materials typically necessitate ingredients that can be polymerized and cross-linked through synthesis of their composition and molecular architecture. In contrast, the concept and manufacturing method used in this work contribute to eliminate the dependence on process parameters and material chemistry, hence making the fabrication compatible with other off-the-shelf materials.

5. Material and methods

5.1. Experimental design

A representative group of materials were chosen for proof-of-concept fabrication, and their temperature-independent CTEs (α) and Young's moduli (E) within a temperature range between 25 and 75 °C were tested with a thermomechanical analyzer (TMA Q400, TA Instrument) and a test machine (313 Family Universal Test Machine, TESTRESOURCES), respectively: Delrin Acetal Resin ($\alpha_{\text{Delrin}} = 9.9 \times 10^{-5} \text{ K}^{-1}$, $E_{\text{Delrin}} = 4693.7 \text{ MPa}$), Ti-6Al-4V ($\alpha_{\text{Ti-6Al-4V}} = 1.0 \times 10^{-5} \text{ K}^{-1}$, $E_{\text{Ti-6Al-4V}} = 106.9 \text{ GPa}$), ULTEM 9085 Resin ($\alpha_{\text{ULTEM 9085}} = 5.8 \times 10^{-5} \text{ K}^{-1}$, $E_{\text{ULTEM 9085}} = 2243.4 \text{ MPa}$). The following are the parameters selected for the unit cell: $l_1 = l_2 = 13 \text{ mm}$, $l_3 = 50 \text{ mm}$, $t_f = 4 \text{ mm}$ (ULTEM 9085 frame), $t_c = 0.7 \text{ mm}$ (Ti-6Al-4V core), and $t_c = 3 \text{ mm}$ (Delrin core). Frames and cores were built separately. For middle-CTE frames (ULTEM 9085), we used Fused Deposition Modeling (FDM) technology, for high-CTE cores (Delrin) laser cutting, and for low-CTE cores (Ti-6Al-4V) wire Electrical Discharge Machining (EDM). The components were then assembled and bonded together with epoxy (Adhaer 5 Min Epoxy Formula Glue).

Thermal testes were conducted in a customized heating chamber with two 200-Watt heaters. The temperature was controlled by a proportion integration differentiation (PID) device (CN7800, OMEGA), and three fans were utilized to provide a uniform heating source. Three thermocouples were placed in different locations in the chamber to measure instant air temperature, and an average was calculated for each group of temperature data. To record the deformation of samples during temperature increases, pictures were captured with a camera (Grasshopper 5.0 MP with Fujinon HF25SA-1 lens) through a transparent glass cover on top of the heating chamber.

5.2. Finite element analyses and point cloud processing

Computational analyses were carried out using the commercial software ABAQUS (Dassault Systèmes Simulia Corp), where the thermal deformation of the lattices was calculated with an implicit solver, and geometric nonlinearity was taken into account in the analyses. Full 3D models of the unit cell, morphing on target lattice, polymorphing lattice, and testing samples were simulated under thermal loads. The Young's moduli and CTEs of the materials used in finite element method simulations were assumed to remain in the elastic regime: (1) 3.1 GPa and $14.9 \times 10^{-5} \text{ K}^{-1}$, (2) 2.2 GPa and $6.5 \times 10^{-5} \text{ K}^{-1}$, and (3) 113.8 GPa and $0.92 \times 10^{-5} \text{ K}^{-1}$. We employed eight-node linear elements (element type C3D8R) with mesh size equal to a quarter of the frame thickness to discretize the models after mesh convergence study. The uniformly applied thermal load of heating throughout the simulations is 120 °C, and the uniform cooling applied to the target lattice for polymorphing I retrieval is −60 °C, followed by polymorphing II under local heating of +50 °C. The 3D coordinates of the midpoint on the top surface of vertical frames were collected from the deformed models for curvature calculations in the material and geometry space, as well as comparison to the target shape. The Abaqus Scripting Interface was used, where Python scripts were developed for the parametric analysis (material and geometry space) and to automatically assemble unit cells with programmed material and geometry into integral encoded lattices such as the one in Fig. 4c.

CloudCompare, an open source 3D point cloud processing software, was used to process the extracted point cloud of deformed lattices and quantify the difference between the point cloud and target mesh for error analysis. Details are presented in the Supplementary Note 3.5.

Declaration of Competing Interest

The authors declare that they have no known competing financial interests or personal relationships that could have appeared to influence the work reported in this paper.

CRediT authorship contribution statement

Ruizhe Ma: Conceptualization, Methodology, Software, Writing – original draft, Writing – review & editing. **Lu Liu:** Software, Investigation. **Omar Wyman:** Investigation, Writing – review & editing. **Damiano Pasini:** Conceptualization, Methodology, Investigation, Writing – original draft, Writing – review & editing, Supervision, Funding acquisition.

Acknowledgements

DP acknowledges the support of the Natural Sciences and Engineering Research Council of Canada [Grant # 208241] and the Canadian Research Chairs program [Grant # 257679].

Data availability

All data used to generate these results is available in the main text or Supplementary Information. Further details could be obtained from the corresponding authors upon reasonable request.

Supplementary materials

Supplementary material associated with this article can be found, in the online version, at doi:[10.1016/j.apmt.2022.101432](https://doi.org/10.1016/j.apmt.2022.101432).

References

- [1] C. Dawson, J.F.V. Vincent, A.M. Rocca, How pine cones open, *Nature* 390 (6661) (1997) 668, doi:[10.1038/37745](https://doi.org/10.1038/37745).
- [2] Y. Forterre, J.M. Skotheim, J. Dumais, L. Mahadevan, How the venus flytrap snaps, *Nature* 433 (7024) (2005) 421, doi:[10.1038/nature03185](https://doi.org/10.1038/nature03185).
- [3] H. Xu, A. Farag, R. Ma, D. Pasini, Thermally actuated hierarchical lattices with large linear and rotational expansion, *J. Appl. Mech.* 86 (11) (2019), doi:[10.1115/1.4044026](https://doi.org/10.1115/1.4044026).
- [4] H. Xu, A. Farag, D. Pasini, Multilevel hierarchy in bi-material lattices with high specific stiffness and unbounded thermal expansion, *Acta Mater.* 134 (2017) 155, doi:[10.1016/j.actamat.2017.05.059](https://doi.org/10.1016/j.actamat.2017.05.059).
- [5] T. Chen, K. Shea, An autonomous programmable actuator and shape reconfigurable structures using bistability and shape memory polymers, *3D Print. Addit. Manuf.* 5 (2) (2018) 91, doi:[10.1089/3dp.2017.0118](https://doi.org/10.1089/3dp.2017.0118).
- [6] L. Liu, C. Qiao, H. An, D. Pasini, Encoding kirigami bi-materials to morph on target in response to temperature, *Sci. Rep.* 9 (1) (2019) 19499, doi:[10.1038/s41598-019-56118-2](https://doi.org/10.1038/s41598-019-56118-2).
- [7] J.H. Na, A.A. Evans, J. Bae, M.C. Chiappelli, C.D. Santangelo, R.J. Lang, T.C. Hull, R.C. Hayward, Programming reversibly self-folding origami with micropatterned photo-crosslinkable polymer trilayers, *Adv. Mater.* 27 (1) (2015) 79, doi:[10.1002/adma.201403510](https://doi.org/10.1002/adma.201403510).
- [8] M.T. Tolley, S.M. Felton, S. Miyashita, D. Aukes, D. Rus, R.J. Wood, Self-folding origami: shape memory composites activated by uniform heating, *Smart Mater. Struct.* 23 (9) (2014) 094006, doi:[10.1088/0964-1726/23/9/094006](https://doi.org/10.1088/0964-1726/23/9/094006).
- [9] A. Kotikian, C. McMahan, E.C. Davidson, J.M. Muhammad, R.D. Weeks, C. Daraio, J.A. Lewis, Untethered soft robotic matter with passive control of shape morphing and propulsion, *Sci. Robot.* 4 (33) (2019) eaax7044, doi:[10.1126/scirobotics.aax7044](https://doi.org/10.1126/scirobotics.aax7044).
- [10] B. Deng, L. Chen, D. Wei, V. Tournat, K. Bertoldi, Pulse-driven robot: motion via solitary waves, *Sci. Adv.* 6 (18) (2020) eaaz1166, doi:[10.1126/sciadv.aaz1166](https://doi.org/10.1126/sciadv.aaz1166).
- [11] R. Guseinov, C. McMahan, J. Pérez, C. Daraio, B. Bickel, Programming temporal morphing of self-actuated shells, *Nat. Commun.* 11 (1) (2020) 237, doi:[10.1038/s41467-019-14015-2](https://doi.org/10.1038/s41467-019-14015-2).
- [12] Y. Mao, K. Yu, M.S. Isakov, J. Wu, M.L. Dunn, H.J. Qi, Sequential self-folding structures by 3D printed digital shape memory polymers, *Sci. Rep.* 5 (1) (2015) 13616, doi:[10.1038/srep13616](https://doi.org/10.1038/srep13616).
- [13] H. Zhang, J. Wu, D. Fang, Y. Zhang, Hierarchical mechanical metamaterials built with scalable tristable elements for ternary logic operation and amplitude modulation, *Sci. Adv.* 7 (9) (2021) eabf1966, doi:[10.1126/sciadv.abf1966](https://doi.org/10.1126/sciadv.abf1966).
- [14] Y. Jiang, L.M. Korpas, J.R. Raney, Bifurcation-based embodied logic and autonomous actuation, *Nat. Commun.* 10 (1) (2019) 128, doi:[10.1038/s41467-018-08055-3](https://doi.org/10.1038/s41467-018-08055-3).

- [15] R. Fernandes, D.H. Gracias, Self-folding polymeric containers for encapsulation and delivery of drugs, *Adv. Drug Deliv. Rev.* 64 (14) (2012) 1579, doi:[10.1016/j.addr.2012.02.012](https://doi.org/10.1016/j.addr.2012.02.012).
- [16] Y. Qiu, K. Park, Environment-sensitive hydrogels for drug delivery, *Adv. Drug Deliv. Rev.* 53 (3) (2001) 321, doi:[10.1016/S0169-409X\(01\)00203-4](https://doi.org/10.1016/S0169-409X(01)00203-4).
- [17] C.L. Randall, E. Gultepe, D.H. Gracias, Self-folding devices and materials for biomedical applications, *Trends Biotechnol.* 30 (3) (2012) 138, doi:[10.1016/j.tibtech.2011.06.013](https://doi.org/10.1016/j.tibtech.2011.06.013).
- [18] H. Meng, G. Li, A review of stimuli-responsive shape memory polymer composites, *Polymer* 54 (9) (2013) 2199 (Guildf), doi:[10.1016/j.polymer.2013.02.023](https://doi.org/10.1016/j.polymer.2013.02.023).
- [19] X. Lan, Y. Liu, H. Lv, X. Wang, J. Leng, S. Du, Fiber reinforced shape-memory polymer composite and its application in a deployable hinge, *Smart Mater. Struct.* 18 (2) (2009) 024002.
- [20] S. Felton, M. Tolley, E. Demaine, D. Rus, R. Wood, A method for building self-folding machines, *Science* 345 (6197) (2014) 644, doi:[10.1126/science.1252610](https://doi.org/10.1126/science.1252610).
- [21] T. Chen, O.R. Bilal, K. Shea, C. Daraio, Harnessing bistability for directional propulsion of soft, untethered robots, *Proc. Natl. Acad. Sci. U. S. A.* 115 (22) (2018) 5698, doi:[10.1073/pnas.1800386115](https://doi.org/10.1073/pnas.1800386115).
- [22] J. Guan, H. He, D.J. Hansford, L.J. Lee, Self-folding of three-dimensional hydrogel microstructures, *J. Phys. Chem. B* 109 (49) (2005) 23134, doi:[10.1021/jp054341g](https://doi.org/10.1021/jp054341g).
- [23] S. Timoshenko, Analysis of Bi-metal thermostats, *J. Opt. Soc. Am.* 11 (3) (1925) 233, doi:[10.1364/JOSA.11.000233](https://doi.org/10.1364/JOSA.11.000233).
- [24] A.I. Egunov, J.G. Korvink, V.A. Luchnikov, Polydimethylsiloxane bilayer films with an embedded spontaneous curvature, *Soft Matter* 12 (1) (2016) 45, doi:[10.1039/C5SM01139F](https://doi.org/10.1039/C5SM01139F).
- [25] W. Guo, M. Li, J. Zhou, Modeling programmable deformation of self-folding all-polymer structures with temperature-sensitive hydrogels, *Smart Mater. Struct.* 22 (11) (2013) 115028, doi:[10.1088/0964-1726/22/11/115028](https://doi.org/10.1088/0964-1726/22/11/115028).
- [26] J. Kim, C. Kim, Y. Song, S.G. Jeong, T.S. Kim, C.S. Lee, Reversible self-bending soft hydrogel microstructures with mechanically optimized designs, *Chem. Eng. J.* 321 (2017) 384, doi:[10.1016/j.cej.2017.03.125](https://doi.org/10.1016/j.cej.2017.03.125).
- [27] S. Alben, B. Balakrishnan, E. Smela, Edge effects determine the direction of bi-layer bending, *Nano Lett.* 11 (6) (2011) 2280, doi:[10.1021/nl200473p](https://doi.org/10.1021/nl200473p).
- [28] M. Finot, S. Suresh, Small and large deformation of thick and thin-film multilayers: effects of layer geometry, plasticity and compositional gradients, *J. Mech. Phys. Solids* 44 (5) (1996) 683, doi:[10.1016/0022-5096\(96\)84548-0](https://doi.org/10.1016/0022-5096(96)84548-0).
- [29] N.J. Salamon, C.B. Masters, Bifurcation in isotropic thinfilm/substrate plates, *Int. J. Solids Struct.* 32 (3) (1995) 473, doi:[10.1016/0020-7683\(94\)00129-K](https://doi.org/10.1016/0020-7683(94)00129-K).
- [30] B.D. Harper, W. Chih-Ping, A geometrically nonlinear model for predicting the intrinsic film stress by the bending-plate method, *Int. J. Solids Struct.* 26 (5) (1990) 511, doi:[10.1016/0020-7683\(90\)90025-Q](https://doi.org/10.1016/0020-7683(90)90025-Q).
- [31] Y. Forterre, J. Dumais, Generating helices in nature, *Science* 333 (6050) (2011) 1715, doi:[10.1126/science.1210734](https://doi.org/10.1126/science.1210734).
- [32] S. Janbaz, R. Hedayati, A.A. Zadpoor, Programming the shape-shifting of flat soft matter: from self-rolling/self-twisting materials to self-folding origami, *Mater. Horiz.* 3 (6) (2016) 536, doi:[10.1039/C6MH00195E](https://doi.org/10.1039/C6MH00195E).
- [33] L.T. de Haan, C. Sánchez-Somolinos, C.M.W. Bastiaansen, A.P.H.J. Schenning, D.J. Broer, Engineering of complex order and the macroscopic deformation of liquid crystal polymer networks, *Angew. Chem. Int. Ed.* 51 (50) (2012) 12469, doi:[10.1002/anie.201205964](https://doi.org/10.1002/anie.201205964).
- [34] J. Kim, J.A. Hanna, R.C. Hayward, C.D. Santangelo, Thermally responsive rolling of thin gel strips with discrete variations in swelling, *Soft Matter* 8 (8) (2012) 2375, doi:[10.1039/C2SM06681E](https://doi.org/10.1039/C2SM06681E).
- [35] Z.L. Wu, M. Moshe, J. Greener, H. Therien-Aubin, Z. Nie, E. Sharon, E. Kumacheva, Three-dimensional shape transformations of hydrogel sheets induced by small-scale modulation of internal stresses, *Nat. Commun.* 4 (1) (2013) 1586, doi:[10.1038/ncomms2549](https://doi.org/10.1038/ncomms2549).
- [36] J.W. Boley, W.M. van Rees, C. Lissandrello, M.N. Horenstein, R.L. Truby, A. Kotikian, J.A. Lewis, L. Mahadevan, Shape-shifting structured lattices via multimaterial 4D printing, *Proc. Natl. Acad. Sci. U.S.A.* 116 (42) (2019) 20856, doi:[10.1073/pnas.1908806116](https://doi.org/10.1073/pnas.1908806116).
- [37] Y. Klein, E. Efrati, E. Sharon, Shaping of elastic sheets by prescription of non-euclidean metrics, *Science* 315 (5815) (2007) 1116, doi:[10.1126/science.1135994](https://doi.org/10.1126/science.1135994).
- [38] J. Kim, J.A. Hanna, M. Byun, C.D. Santangelo, R.C. Hayward, Designing responsive buckled surfaces by halftone gel lithography, *Science* 335 (6073) (2012) 1201, doi:[10.1126/science.1215309](https://doi.org/10.1126/science.1215309).
- [39] S. Xu, Z. Yan, K.I. Jang, W. Huang, H. Fu, J. Kim, Z. Wei, M. Flavin, J. McCracken, R. Wang, A. Badea, Y. Liu, D. Xiao, G. Zhou, J. Lee, H.U. Chung, H. Cheng, W. Ren, A. Banks, X. Li, U. Paik, R.G. Nuzzo, Y. Huang, Y. Zhang, J.A. Rogers, Assembly of micro/nanomaterials into complex, three-dimensional architectures by compressive buckling, *Science* 347 (6218) (2015) 154, doi:[10.1126/science.1260960](https://doi.org/10.1126/science.1260960).
- [40] Y. Sun, W.M. Choi, H. Jiang, Y.Y. Huang, J.A. Rogers, Controlled buckling of semiconductor nanoribbons for stretchable electronics, *Nat. Nanotechnol.* 1 (3) (2006) 201, doi:[10.1038/nnano.2006.131](https://doi.org/10.1038/nnano.2006.131).
- [41] L.H. Dudte, E. Vouga, T. Tachi, L. Mahadevan, Programming curvature using origami tessellations, *Nat. Mater.* 15 (5) (2016) 583, doi:[10.1038/nmat4540](https://doi.org/10.1038/nmat4540).
- [42] P. Celli, C. McMahan, B. Ramirez, A. Bauhofer, C. Naify, D. Hofmann, B. Audoly, C. Daraio, Shape-morphing architected sheets with non-periodic cut patterns, *Soft Matter* 14 (48) (2018) 9744, doi:[10.1039/C8SM02082E](https://doi.org/10.1039/C8SM02082E).
- [43] T. Chen, H. Li, Z. Li, Q. Jin, J. Ji, A "writing" strategy for shape transition with infinitely adjustable shaping sequences and *in situ* tunable 3D structures, *Mater. Horiz.* 3 (6) (2016) 581, doi:[10.1039/C6MH00295A](https://doi.org/10.1039/C6MH00295A).
- [44] S.M. Felton, M.T. Tolley, B. Shin, C.D. Onal, E.D. Demaine, D. Rus, R.J. Wood, Self-folding with shape memory composites, *Soft Matter* 9 (32) (2013) 7688, doi:[10.1039/C3SM51003D](https://doi.org/10.1039/C3SM51003D).
- [45] A. Sydney Gladman, E.A. Matsumoto, R.G. Nuzzo, L. Mahadevan, J.A. Lewis, Biomimetic 4D printing, *Nat. Mater.* 15 (4) (2016) 413, doi:[10.1038/nmat4544](https://doi.org/10.1038/nmat4544).